Communication

Crystallographic Orientation Relationship with Geometrically Necessary Dislocation Accumulation During High-Temperature Deformation in RR1000 Nickel-Based Superalloy

SORAN BIROSCA

In the current study, it is demonstrated that soft grains along ⟨100⟩ fiber provided a pure shear condition for easy dislocation movement leading to a relatively low dislocation density. The hard grains along the ⟨111⟩ fiber, however, were not favorably oriented for slip system activation and caused high dislocation accumulation. It is concluded that the average overall dislocation density does not provide a meaningful value, as it is largely dependent on the original material crystallographic texture, the numbers of hard and soft grains in the electron backscatter diffraction (EBSD) mapped area, and the grain size factor.

https://doi.org/10.1007/s11661-018-5036-y

RR1000 Ni-based superalloys developed at Rolls-Royce are mainly used for turbine discs in the rotational hot sections due to their exceptional high-temperature mechanical properties. However, this alloy is subjected to creep deformation in an oxidizing environment in most of its applications. Therefore, understating the creep deformation mechanism for this alloy under various creep loading conditions is of great industrial and academic research interest. It is widely reported that the failure mechanism is strongly influenced by the microstructure, grain size, grain orientation, grain boundary geometry, second-phase precipitates, porosity, and inclusions.[1–6] For the past 50 years, numerous theoretical, experimental, and computer simulation studies have been conducted on creep deformation of nickel-based superalloys. However, most of the studies in the literature have been based on dislocation-based theories to understand the development, generation, movement, accumulation, and mobility of dislocations during loading. Yet, due to the complexity of the superalloy system, the dislocation plasticity theory cannot portray the complete description of the creep deformation mechanism. This is partly due to the limitations of micro- and nanoanalytical tools to depict the exact behavior of dislocations during high-temperature static loading.[7–9] It is established that the electron backscatter diffraction (EBSD) technique can calculate geometrically necessary dislocation (GND) type but cannot recognize statistically stored dislocation (SSD) type.[10,11] In general, dislocations are stored because they accumulate by trapping each other in a random way, *i.e.*, SSDs, or they are required for compatible deformation of various parts of the material, *i.e.*, GNDs.[12–14] Therefore, SSDs do not contribute to the lattice curvature, *i.e.*, misorientation values. The difficulty in capturing the effect on SSD type using diffraction-based EBSD data is that an SSD dislocation is assumed to move and glide to relax the stress without leaving a geometrical plastic effect in the material.[12] Meanwhile, GNDs align themselves to accommodate the lattice curvature, which clearly has an effective geometric plastic effect and can be directly calculated using EBSD misorientation data.[15] Thus, in the current investigation, an EBSD tool was used for GND behavior observations only to assess the technique capability in creep deformation studies. Sun *et al.*[16] also reported that the lattice curvature was observed near interfaces. They claimed that the GND accumulations at or near grain boundaries were dependent on the strain level imposed on the material. They also showed through experimental study that interfaces can resist the motion of lattice dislocations or absorb or emit them depending upon the structure of the interface and local stress states. Furthermore, Ashby,[17] and recently Zhu *et al.*,[18] demonstrated that, at small strain condition, the dislocation density and, hence, work hardening is controlled by GNDs. At large strain conditions, however, work hardening at the later stage of plastic deformation is mainly controlled by SSDs. They also stated that GNDs dominate the total density at small strains but can be swamped by the SSDs at larger strains. Here, the validity of these postulations is only assessed *via* GND measurement, neglecting SSD contributions on work hardening and strain accumulation at the stress magnitudes used throughout the current study.

The alloy used in this study was nickel-based superalloy RR1000, which was provided by Rolls-Royce, Derby, UK. The chemical composition of the alloy is shown in Table I. The material was isothermally forged from extruded billet, followed by solution (1170 °C/2 h/fan air quenching) and precipitation (760 °C/16 h/air cooling) heat treatments. The average grain size was in the range of 30 ± 5 μm diameter. Dog-bone-shape specimens were produced with a gage length of 10 mm and a width of 5 mm. The creep test was conducted on

SORAN BIROSCA is with the Institute of Structural Materials, College of Engineering, Swansea University, Bay Campus, Swansea SA1 8EN, UK. Contact email: S.Birosca@swansea.ac.uk
Manuscript submitted September 17, 2018.
Article published online December 3, 2018

Table I. Chemical Composition of RR1000 Ni-Based Superalloy (Weight Percent)

Co	Cr	Mo	Ta	Ti	Al	C	B	Zr	Hf
18.5	15	5	2	3.6	3	0.027	0.015	0.06	0.5

RR1000 at 600 MPa/750 °C and 1000 MPa/650 °C, below and above the yield stress of RR1000, respectively. It should be noticed here that the temperatures used at different applied creep stresses are different by 100 °C to approximate the industrial loading conditions for RR1000 in jet engines.

Sectioned specimens were metallographically prepared using the standard method, culminating with 0.05 μm colloidal silica for 20 minutes. Data were collected using a Nordlys EBSD detector and HKL Technology Channel 5 EBSD system interfaced to a Phillips XL30 tungsten electron microscope operated at 20 kV using 15 mm working distance. The orientation data were collected using 200 nm step size in order to determine the orientation spread within individual grains at relatively small length scales. The diffraction pattern binning of 4 × 4 was employed, and the noise floor was calculated using the method described in Reference 19 and is found to be much less than average GND values. Jiang *et al.*[19] demonstrated that, during high-resolution EBSD scan, the noise floor increased with decreasing step size. However, they also showed that in the deformed materials the average GND density stays relatively constant as the degree of pattern binning is increased up from 1 × 1 to 8 × 8,[19] which is the case in this study as the material is crept until failure. In general, using a large step size will reduce the noise level and enable EBSD scanning of larger regions but will result in many GNDs being counted as SSDs; therefore, discrimination of key structures, such as dislocation cell walls, will be less clear.[19] A compromise must be made in the step size selection process as the appropriate step size depends on several factors, such as the original dislocation density stored in samples, angular resolution, and the step size of EBSD maps. When one adjusts these variables, the most important issue is that the measured GND density must be above the noise floor. Thus, in the current study, the EBSD orientation data are collected with a 200 nm step size in order to determine the orientation spread within individual grains at small length scales. This EBSD step size was chosen small enough to be microscopically relevant and large enough to filter out the EBSD noise (averaging the scatter due to EBSD angular resolution limits). The detailed procedure of selecting the correct EBSD scan step size can be found in Reference 20. The EBSD obtained data were then analyzed using the HKL-Channel 5 analysis packages. The GND maps were generated from EBSD raw data using in-house python code. The principles and methodology of GND calculation are already reported in References 21 and 22.

Figure 1 shows the EBSD characterization of the sample crept below the yield stress of RR1000, *i.e.*, 600 MPa at 750 °C. The average grain size is 30 ± 5 μm (Figure 1(a)). However, there are two main size clusters of the grains: 40 ± 5 μm in diameter (~ 65 pct) and 20 ± 5 μm in diameter (~ 35 pct); they do not create an ideal necklace microstructure but rather are randomly distributed. Figure 1(b) shows the inverse pole figure (IPF)/loading direction (LD). The ideal grain orientation and fiber texture maps as well as orientation distribution function (ODF) plots are shown in Figures 1(c) and (d). It is clear from the figures that no strong texture was exhibited in the alloy, and the texture components, including cube, Goss, brass, and copper, are randomly distributed within the microstructure (Figure 1(c)). However, the three main fiber textures of $\langle 100\rangle//Y$, $\langle 110\rangle//Y$, and $\langle 111\rangle//Y$ dominate the orientation populations with the highest area fraction of 30 pct for the latter fiber texture (Figure 1(d)). It should be noted here that the *Y*-axis is parallel to the LD. Furthermore, the majority of the grains on the $\langle 111\rangle//Y$ fiber have a low Schmid factor (SF) (0.23 to 0.34: hard grains) and contain high GND density ($10^{3.4}$ to $10^{3.6}$ μ/μ^3) (Figure 1(e) and the black elliptical shapes on the GND map in Figure 1(f)), respectively, whereas ~ 75 pct of the grains on the $\langle 100\rangle//Y$ fiber have high SF (0.4 to 0.49: soft grains) and contain low GND density ($10^{2.2}$ to $10^{2.7}$ μ/μ^3) (Figure 1(e) and red elliptical shapes on the GND map in Figure 1(f), respectively). However, the grains on the $\langle 110\rangle//Y$ fiber were found to be within both soft and hard classified grain groups. They could have high SF and low GND density or *vice versa*, depending on the neighboring grain orientations and grain sizes. For further clarification, Figure 3 shows an ideal soft grain exhibiting a high SF of 0.48 and low average GND density of $10^{2.3}$ μ/μ^3 (Figures 3(a) through (c)), whereas a hard grain exhibited a low SF of 0.32 and a high average GND density of $10^{3.5}$ μ/μ^3 (Figures 3(d) through (f)). For SF mapping, the *Y*-axis is aligned with the LD in Figure 1(a) and only an octahedral slip system (111) $\langle 1\bar{1}0\rangle$ was considered.

A similar observation was found in the RR100 specimen crept above the yield stress of the alloy, *i.e.*, 1000 MPa at 650 °C (Figures 2(a) through (f)). It should be emphasized here, comparing the two crept samples, that the 1000 MPa sample contained more grains on the $\langle 111\rangle//Y$ fiber (33 pct area fraction) and much fewer grains on the $\langle 100\rangle//Y$ fiber (13 pct area fraction) with a minimum number of grains on the $\langle 110\rangle//Y$ fiber (only 6 pct). This means that the 1000 MPa sample contained a greater number of hard grains and fewer soft grains than the 600 MPa sample. Therefore, it is not surprising to observe a much lower overall SF value (*i.e.*, 0.35) and higher overall GND density (*i.e.*, $10^{3.5}$ μ/μ^3) in the 1000 MPa sample than in the 600 MPa sample, which has a high 0.43 overall SF and overall GND density value of $10^{2.6}$ μ/μ^3. Hence, it is concluded that the overall GND density and average SF

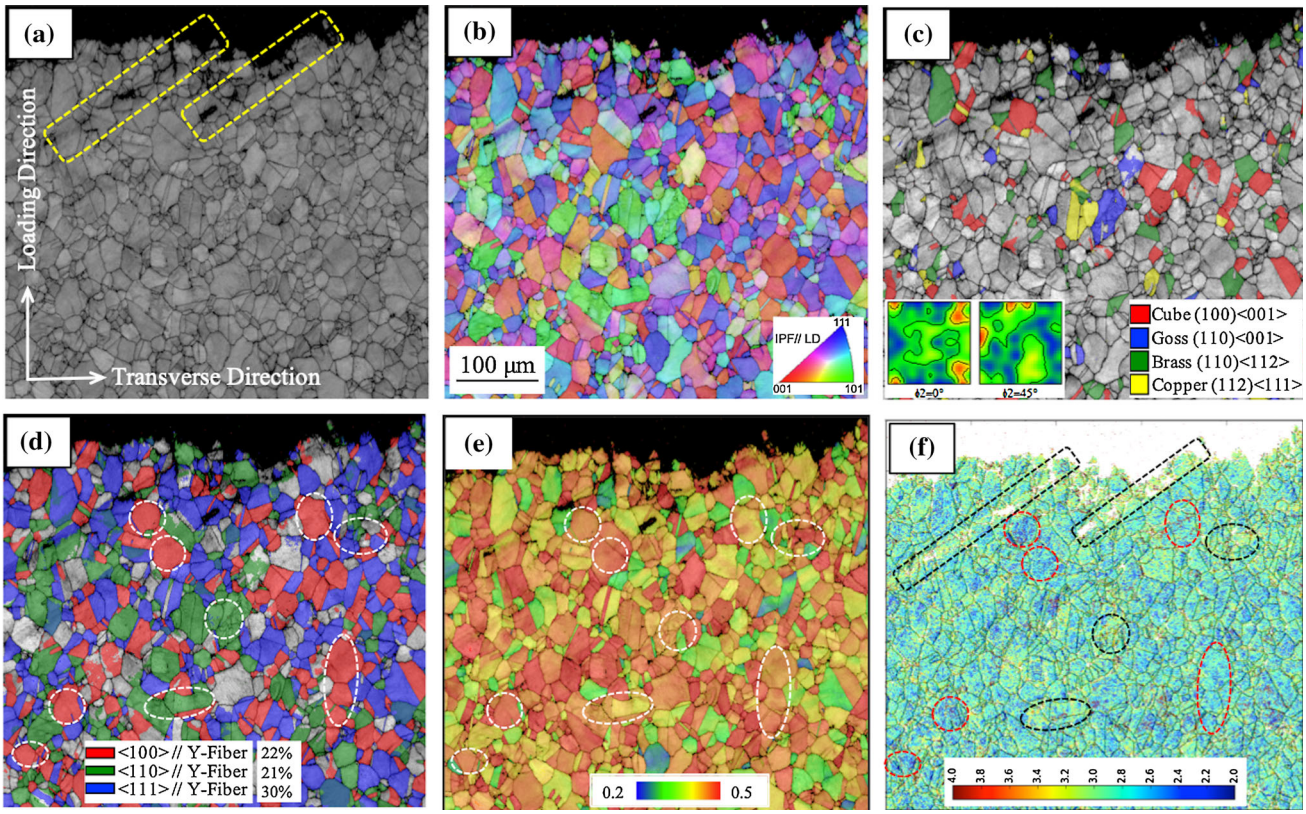

Fig. 1—RR1000 nickel-based superalloy following creep test at 600 MPa/750 °C: (*a*) EBSD-HKL derived BC map; (*b*) EBSD-HKL derived IPF// LD (*Y*-axis) map; (*c*) EBSD-HKL derived texture component map; (*d*) EBSD-HKL derived texture fiber map; (*e*) EBSD-HKL derived (111) $\langle 1\bar{1}0 \rangle$ SF map, LD = *Y*-axis; and (*f*) GND two-dimensional (2-D) map: 200 nm step size is used. The black and red elliptical shapes in (f) highlight a few hard and soft grains, respectively. The dashed yellow rectangular shapes in (a) highlight the secondary crack direction (Color figure online).

values of the samples might give inaccurate quantitative data comparison between different crept samples, as they largely depend on the original material texture and the number of hard and soft grains mapped during EBSD scans. Thus, care should be taken in comparing these deformed samples and the original material texture must be considered for such a comparison. For instance, the original 600 MPa/750 °C sample has a relatively strong Cube (100) ⟨001⟩ texture component (ODFs in Figure 1(c)), which indicates recrystallization occurrence in this sample (*i.e.*, part of the disc from which the sample was taken). The sample also contained weak brass (110) ⟨112⟩ and copper (112) ⟨111⟩ texture components that are typical fcc material deformation texture components, whereas the 1000 MPa/650 °C sample exhibited weak Cube and relatively strong brass and S texture components (ODFs in Figure 2(c)). The original texture exhibited in the untested materials prior to the loading indeed permitted different numbers of soft and hard grains to be mapped during the EBSD scans. Hence, the SF and GND density values varied depending on the EBSD scan area and the part of the disc that was examined. Nevertheless, the reduced image quality and the EBSD diffraction pattern band contrast (BC) in the 1000 MPa sample with an average BC value of 95 (Figure 2(a)), compared to a much higher value of BC in the 600 MPa sample (average BC value of 185), indicates a much higher strained condition in the former. It should be remembered here that BC is an EBSD diffraction pattern quality factor derived from the Hough transform data, which describes the average intensity of the Kikuchi bands with respect to the overall intensity within the EBSP. The values are normally scaled to a byte range from 0 to 255 (*i.e.*, low to high contrast).

Furthermore, as highlighted in Figure 1(a), two secondary cracks were generated diagonally to the propagating primary crack front. Secondary crack formation perpendicular to the main primary crack is expected during the late stage of creep deformation. As shown in Figure 1(f), the GND around the secondary cracks is higher than the surrounding area and that may affect the overall GND value in the sample. However, the secondary crack formation was not unique in the sample crept at 600 MPa but also occurred in the sample crept at 1000 MPa (the dashed white rectangular shape in Figure 2(b)). These secondary cracks are integral parts of the microstructure alteration during the late creep loading stage; thus, they should be included in the overall GND density without extracting the GND data surrounding the cracks. However, during the original GND calculation, the poor indexing diffraction pattern was extracted from the data set. As shown in Figures 1(f) and 2(f), the secondary crack widths and surrounding areas are not considered in the GND calculations and appeared as a white background

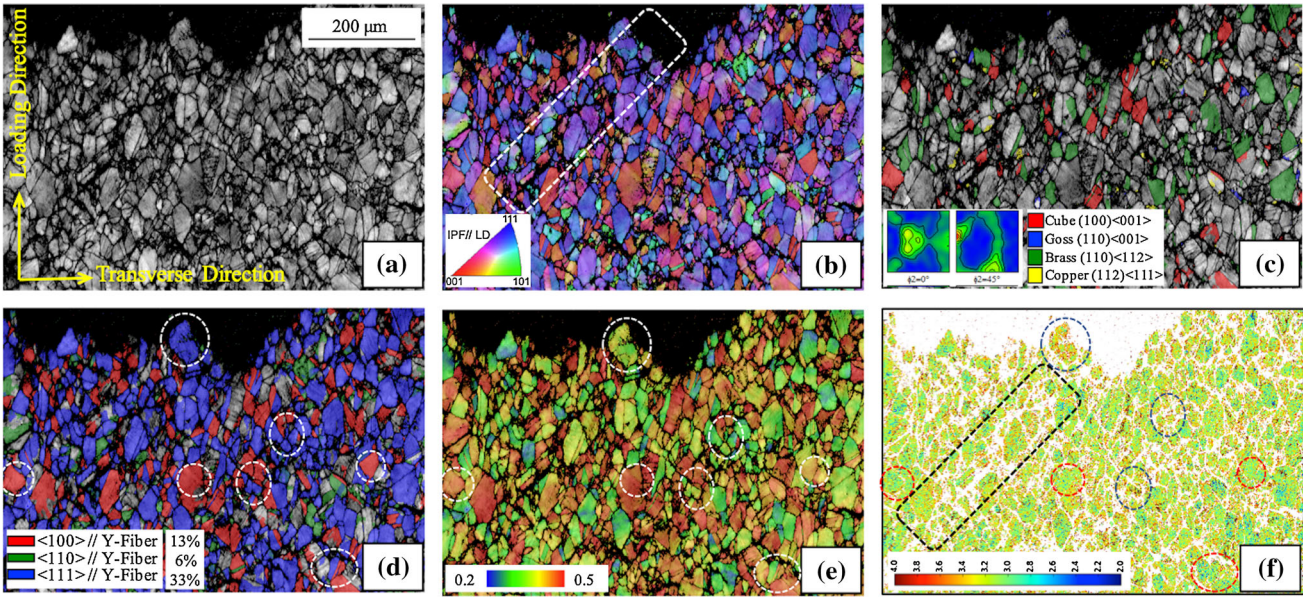

Fig. 2—RR1000 nickel-based superalloy following creep test at 1000 MPa/650 °C: (*a*) EBSD-HKL derived BC map; (*b*) EBSD-HKL derived IPF//LD (*Y*-axis) map; (*c*) EBSD-HKL derived texture component map; (*d*) EBSD-HKL derived texture fiber map; (*e*) EBSD-HKL derived (111) $\langle 1\bar{1}0 \rangle$ SF map, LD = *Y*-axis; and (*f*) GND 2D map: 200 nm step size is used. The dark blue and red elliptical shapes in (f) highlight a few hard and soft grains, respectively. The dashed white rectangular shape in (b) highlights the secondary crack direction (Color figure online).

on the GND maps. Moreover, in the studied samples, much larger areas were scanned and the crack area covered less than 3 pct of the overall sample area. Therefore, the contribution of relatively high GND density around the cracks to the overall GND density is not significant. Nevertheless, the secondary crack formation along with the crystallographic orientation and grain size might affect the overall GND density to some extent; hence, greater care should be taken in using overall GND density values for comparing different deformed samples.

It is evident from Figures 1 and 2 that the hard and soft grains work differently under creep loading, which resulted in heterogeneous strain distribution and GND accumulation depending on the percent of different grain orientations. This is consistent with the previous study on RR1000 during thermomechanical fatigue testing.[21–23] As postulated in Reference 21 and demonstrated and validated here, the octahedral slip system in the soft grain can be easily activated (high SF) and this can facilitate uniform pure shear condition and an easy yield for the soft grains without the need for grain reorientation. Moreover, the pure shear condition in soft grains allows unrestricted movement of dislocations on (111) slips. This results in low GND accumulation in the soft grains, while, in hard grains, *i.e.*, those not favorably oriented for octahedral slip system activation (low SF), the grain tends to rotate to activate any of the available slip systems. This causes dislocation generation on different slip planes. Eventually, the hard grains resist the crystal rotation through accommodating further GND, causing strain hardening of the material. This leads to high GND accumulation within the hard grains. Therefore, the average GND value of a particular sample would change considerably depending on the EBSD scan area and sample location cut from the RR1000 disc.

As discussed earlier, the average overall GND densities in the RR1000 sample crept below and above the yield stress were $\sim 10^{2.6}$ and $10^{3.5}$ μ/μ^3, respectively (Figures 1(f) and 2(f)). This is related to the fact that creep below the yield stress of RR1000 nickel-based superalloy would not generate new dislocations in all differently oriented grains and only the pre-existing dislocation would move depending on the applied macroscopic stress and grain orientations. Thus, the pre-existing dislocation would move until reaching the grain boundaries and entangle, causing GND accumulation depending on the grain orientation, as previously discussed, whereas the creep above the yield stress of RR1000, *i.e.*, 1000 MPa, would generate a large number of new dislocations in nearly all differently orientated grains and, with the pre-existing dislocation movement, can cause larger dislocation accumulation within the individual grains. Although the results reported in the current study can be validated *via* dislocation-based theory, the number of EBSD mapped grains and their orientation should be considered carefully during overall GND and average SF sample comparison. Based on the preceding reported results, the following conclusions are drawn.

1. It was evident from the overall statistical analysis that the grains on $\langle 100 \rangle$-fiber (including Cube and Goss family orientations) acted as "soft" grains (high SF) and contained low GND density, whereas the grains on $\langle 111 \rangle$-fiber (including brass and copper family orientations) acted as "hard" grains that have low SF with high GND density.

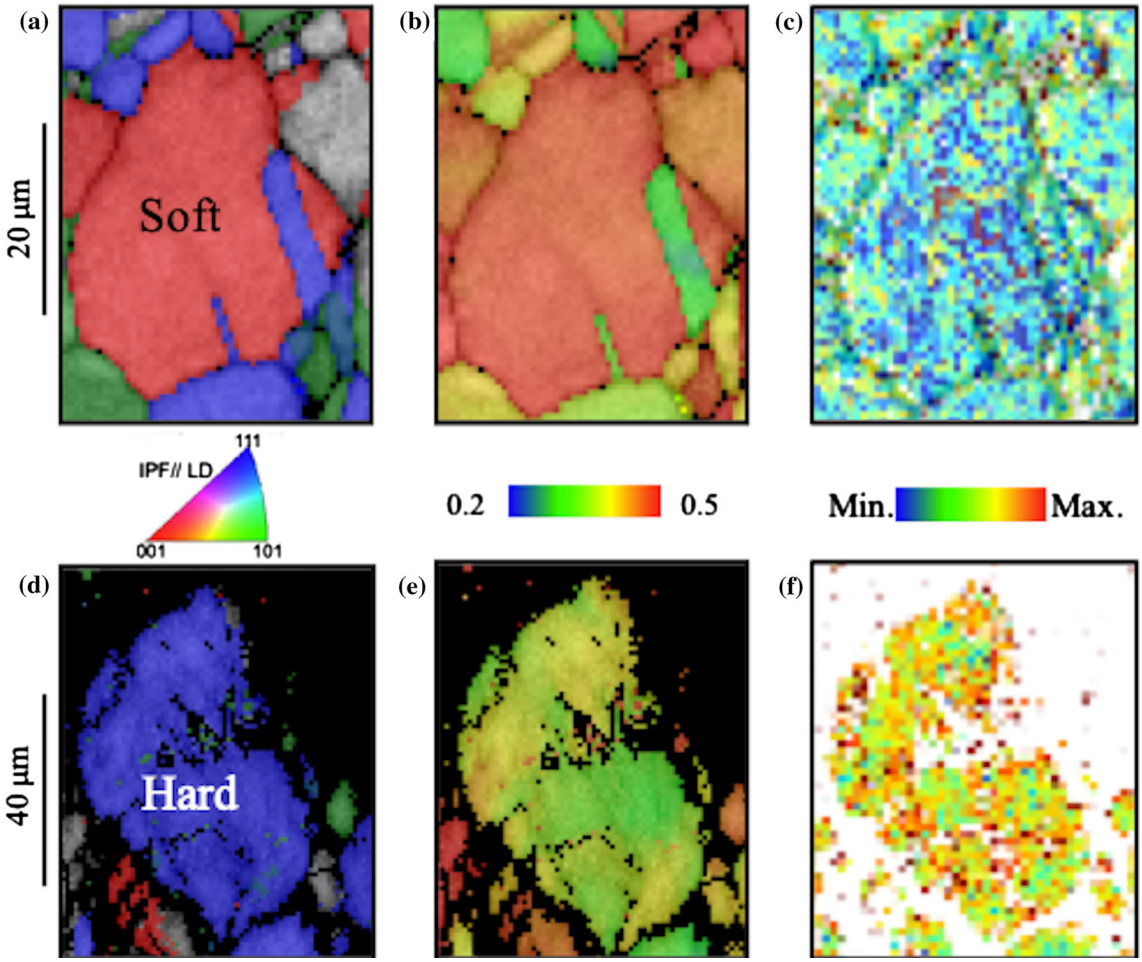

Fig. 3—(*a*) and (*d*) EBSD-HKL derived IPF//LD (*Y*-axis) map; (*b*) and (*e*) EBSD-HKL derived (111) $\langle 1\bar{1}0 \rangle$ SF map, LD = *Y*-axis; and (*c*) and (*f*) GND 2D map: 200 nm step size is used for a soft grain in (a) and a hard grain in (d).

2. It is demonstrated that during creep testing below the yield stress of RR1000 at 600 MPa/750 °C, the strain hardening *via* dislocation entanglement depends on the pre-existing dislocation movement on available slip systems in some oriented grains. Moreover, due to insufficient microscopic stress level, the GND accumulation is relatively low, whereas, in addition to the movement of the pre-existing dislocation and higher mobility rate under 1000 MPa/650 °C creep condition, a large number of dislocations were generated in nearly all differently oriented grains and moved, which resulted in much higher GND density in the overall sample. It appears the continuous generation of the dislocations under 1000 MPa creep condition contributed greatly in higher strain hardening than in the 600 MPa crept sample, which is also indicated on EBSD BC maps.
3. It is concluded that the average GND density value comparison between 600 and 1000 MPa crept samples does not provide meaningful comparative data. This is related to the fact that the average GND values cannot be representative, as is totally dependent on the original crystallographic texture, numbers of hard and soft grains in the EBSD scanned area, crack and defect presence, in addition to the grain size factor.

The current research was funded under the EPSRC Rolls-Royce Strategic Partnership in Structural Metallic Systems for Gas Turbines (Grant Nos. EP/H500383/1 and EP/H022309/1").

OPEN ACCESS

REFERENCES

1. F. Daus, H.Y. Li, G. Baxter, S. Bray, and P. Bowen: *Mater. Sci. Technol.*, 2007, vol. 23 (12), pp. 1424–32.
2. D.M. Knowles and D.W. Hunt: *Metall. Mater. Trans. A*, 2002, vol. 33A, pp. 3165–72.
3. B. Lin, L.G. Zhao, and J. Tong: *Eng. Fract. Mech.*, 2011, vol. 78, pp. 2174–92.
4. B. Lin, L.G. Zhaoa, J. Tonga, and H.-J. Christ: *Mater. Sci. Eng. A*, 2010, vol. 527, pp. 3581–87.
5. D. Turan, D. Hunt, and D.M. Knowles: *Mater. Sci. Technol.*, 2007, vol. 23 (2), pp. 183–88.
6. H.T. Pang and P.A.S. Reed: *Int. J. Fatigue*, 2003, vol. 25, pp. 1089–99.
7. C. Rae and R. Reed: *Acta Mater.*, 2007, vol. 55, pp. 1067–81.
8. F. Pyczak, B. Devrient, F. Neuner, and H. Mughrabi: *Acta Mater.*, 2005, vol. 53 (14), pp. 3879–91.
9. J. Wosik, B. Dubiel, A. Kruk, H. Penkalla, F. Schubert F. Czyrska: *Mater. Charact.*, 2001, vol. 46 (2), pp. 119–23.
10. W. Pantleon: *Scripta Mater.*, 2008, vol. 58, pp. 994–97.
11. J. Jiang, B. Britton, and A. Wilkinson: *Acta Mater.*, 2013, vol. 61, pp. 7227–39.
12. H. Gao, Y. Huang, W. Nix, and J. Hutchinson: *J. Mech. Phys. Solids*, 1999, vol. 47, pp. 1239–63.
13. H. Gao and Y. Huang: *Scripta Mater.*, 2003, vol. 48, pp. 113–18.
14. Y. Guo, B. Britton, and A. Wilkinson: *Acta Mater.*, 2014, vol. 76, pp. 1–12.
15. A. Arsenlis and D. Parks: *Acta Mater.*, 1999, vol. 47 (5), pp. 1597–611.
16. S. Sun, B. Adams, and W.E. King: *Phil. Mag.*, 2000, vol. 80 (1), pp. 9–25.
17. M. Ashby: *Phil. Mag.*, 1970, vol. 21 (170), pp. 399–424.
18. C. Zhu, T. Harrington, G. Gray, III, and K. Vecchio: *Acta Mater.*, 2018, vol. 155, pp. 104–16.
19. J. Jiang, T.B. Britton, and A.J. Wilkinson: *Ultramicroscopy*, 2013, vol. 125, pp. 1–9.
20. D. Kerr: Ph.D. Thesis, Swansea University Library, United Kingdom, 2013.
21. S. Birosca, F. Gioacchino, S. Stekovic, and M. Hardy: *Acta Mater.*, 2014, vol. 74, pp. 110–24.
22. G. Liu, J. Salvat Canto, S. Winwood, K. Rhodes, and S. Birosca: *Acta Mater.*, 2018, vol. 148, pp. 391–406.
23. S. Birosca: *IOP Conf. Series: Materials Science and Engineering, ICOTOM-17 Conf. Proc., 17th Int. Conf. on Texture of Materials*, Dresden, Germany, IOP Publishing. 2015, vol. 82. p. 012033.